THE JOURNAL OF PHYSICAL CHEMISTRY C
A JOURNAL OF THE AMERICAN CHEMICAL SOCIETY

pubs.acs.org/JPCC

Article

Machine Learning, Density Functional Theory, and Experiments to Understand the Photocatalytic Reduction of CO_2 on CuPt/TiO_2

Vaidish Sumaria, Takat B. Rawal,* Young Feng Li, David Sommer, Jake Vikoren, Robert J. Bondi, Matthias Rupp, Amrit Prasad, and Deeptanshu Prasad

Cite This: *J. Phys. Chem. C* 2024, 128, 14247−14258

Read Online

ACCESS | Metrics & More | Article Recommendations | Supporting Information

ABSTRACT: The photoconversion of CO_2 to hydrocarbons is a sustainable route for its transformation into value-added compounds, which is crucial to mitigating energy and climate crises. CuPt nanoparticles on TiO_2 surfaces have been reported to show promising photoconversion efficiencies. For further progress, a mechanistic understanding of the catalytic properties of these CuPt/TiO_2 systems is vital. Here, we employ *ab initio* calculations, machine learning, and photocatalysis experiments to understand the photocatalytic reduction of CO_2 on CuPt/TiO_2. We explore the configurational space of the CO_2@CuPt/TiO_2 systems and examine their structures and energetics. We find that the CuPt/TiO_2 interface plays a key role in determining CO_2 activation and, thus, the conversion to hydrocarbons. The interface stabilizes *CO and other intermediates containing CH groups, thus facilitating a higher activity and selectivity for methane. A bias-corrected machine-learning interatomic potential trained on density functional theory data enables the efficient exploration of the potential energy surfaces of numerous CO_2@CuPt/TiO_2 configurations using basin-hopping Monte Carlo simulations, greatly accelerating the study of these photocatalyst systems. Our simulations show that CO_2 preferentially adsorbs at the interface, with a C atom bonded to a Pt site and one O atom occupying an O-vacancy site. The interface also promotes the formation of *CH and *CH_2 intermediates. For confirmation, we synthesize CuPt/TiO_2 samples with various compositions, analyze their morphologies and compositions using scanning electron microscopy and energy-dispersive X-ray spectroscopy, and measure their photocatalytic activity. Our computational and experimental findings qualitatively agree and highlight the importance of the interface design for the selective conversion of CO_2 to hydrocarbons.

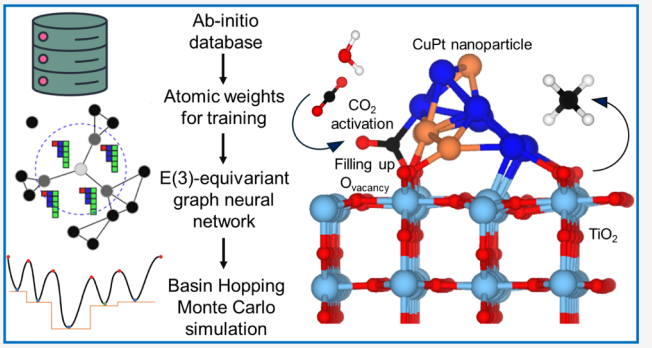

INTRODUCTION

The efficient conversion of CO_2 into value-added products is an important step in mitigating energy and climate crises. CO_2-derived chemicals, such as polycarbonates and urea, as well as fuels, such as methane, alcohol, and jet fuel, have industrial applications and thus can provide routes for monetization. Owing to its natural abundance, low operating costs, high chemical stability, low toxicity, and environmental compatibility, TiO_2 and its derived materials have been extensively investigated over roughly seven decades, with several promising applications,[1−4] including catalysis[5−9] and photocatalysis.[10−13] Using mechanistic insights to rationally optimize TiO_2-based materials is fundamental to enhance the CO_2-capture efficiency and improve the activity and selectivity for its conversion to hydrocarbons.

Despite the challenges of low yields ($\sim\mu mol^{-1}\cdot g^{-1}hr^{-1}$) for large-scale applications in photocatalytic CO_2 conversion to hydrocarbons, the activity and selectivity of TiO_2-based systems[13−16] are encouraging. Since pristine TiO_2 suffers from a low yield due to several reasons, including the maximum-visible light under-utilization,[17] large electron−hole separation,[10] and wide band gaps ~3.0 eV (rutile)[18] and 3.2 eV (anatase),[19] several strategies have been tested insofar. Manipulating the geometric/electronic properties of TiO_2 via the creation of oxygen vacancies or depositing metal (e.g., Cu/Pt) nanoparticles have the potential to enhance the photocatalytic activity.[20]

On TiO_2 surfaces, CO_2 activation is a bottleneck step for various reasons.[21−24] For instance, *CO_2 formation via absorption of photoexcited electrons ($CO_{2(g)} + e^- \rightarrow *CO_2$) is thermodynamically hindered, while *CHOO formation via absorption of two electrons ($CO_{2(g)} + H + 2e^- \rightarrow *CHOO$) is kinetically hindered.[24] The trivial charge transfer between *CO_2

Received: April 7, 2024
Revised: July 30, 2024
Accepted: August 5, 2024
Published: August 15, 2024

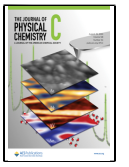

https://doi.org/10.1021/acs.jpcc.4c02275
J. Phys. Chem. C 2024, 128, 14247−14258

and TiO_2 would result in weaker interactions.[21−23] Since CO_2 weakly interacts with defect-laden TiO_2 (see Supporting Information), it cannot facilitate CO_2 activation without an external driving force, thus necessitating the engineering of TiO_2 structures.

Manipulation of the geometrical and electronic structures of TiO_2-based systems has a remarkable impact on their chemical activity. Under reducing conditions, a TiO_2 surface contains O vacancies that bolster metal−support interactions and enhance its reactivity.[25,26] The Cu-decorated TiO_{2-x} promotes CO_2 conversion.[27] The suitable band realignment due to charge transfer[28] enhances the activity of Pt/TiO_2 for CO_2 conversion to CH_4.[29] $CuPt/TiO_2$ shows better activity than Pt/TiO_2.[30] $CuPt/TiO_2$ offers good activity toward the photocatalytic CO_2 conversion and higher selectivity for CH_4 (yield ∼92%).[13] For rutile TiO_2, the {110} surface is the most energetically stable facet.[31] In this work, we model $CuPt/TiO_2$ systems by considering the rutile TiO_2(110) with an O vacancy and 13-atom CuPt clusters.

For the accelerated discovery of materials for CO_2 reduction, various machine-learning (ML) models have been utilized to study several systems,[32−35] including (bare) semiconductor oxides.[33] More recently, the E(3)-equivariant neural network (ENN) has attracted attention owing to the high data efficiency of ML models.[36,37] The ML approach, in combination with the basin-hopping Monte Carlo (BHMC) method, can provide an efficient way to tackle the combinatorial problem of the composition of bimetallic CuPt nanoclusters together with CO_2 adsorbates, which is related to the large degrees of freedom due to several adsorption sites and the orientation of clusters and CO_2.

While *ab initio* methods offer atomistic insights into the potential energy surface (PES) of material systems, they suffer from high computational cost and inefficient scaling with system sizes; ML interatomic potentials (MLIPs) can provide substantial speed-ups at the expense of accuracy with linear scaling. ML can often reduce computational costs by orders of magnitude.[38,39] MLIPs have been improved drastically to achieve higher accuracy in energies (<1 meV/atom) and forces (<0.1 eV/Å) and have been utilized in several applications, e.g., in understanding complex materials chemistry,[40−45] enumerating nanostructure configurations,[42,46] performing long-time MD simulations,[47−49] and exploring catalytic reactions.[50−53] Nevertheless, the training of MLIPs faces challenges of inherent biases due to uneven sampling of training data sets. Such problems arise because the data sets typically contain mostly repeating bulk atomic structures, but less common structures, like surfaces with low coordination, defects on surfaces, and adsorbates on surfaces, are underrepresented. The data sets involving such an inhomogeneous atomic environment cause inaccuracy in the MLIP model. The MLIP behaves as highly accurate for well-represented bulk atomic structures but produces errors for underrepresented configurations. To develop an accurate MLIP model for the simulation of CO_2@$CuPt/TiO_2$ systems, it is therefore important to correct these biases.

Herein, we perform *ab initio* calculations of $Cu_{(13-n)}Pt_n/TiO_2$(110) model systems to generate the atomic coordinates, energy, and forces for the initial training of MLIP based on ENN.[37] We modify the algorithm to reduce unwanted errors in underrepresented configurations using the Gaussian density function-based weighting scheme, improving MLIP reliability and transferability. We use an unbiased MLIP together with the BHMC algorithm to enumerate several configurations of CO_2@$Cu_{(13-n)}Pt_n/TiO_2$ and find that CO_2 adsorbs at interfacial sites. CO_2 activation is then validated by DFT calculations of the adsorption energy, CO_2 bond length/angle changes, and charge transfer. Having examined the key reaction pathways for the overall reaction between CO_2 and H_2O, we provide mechanistic insights into the role of the $CuPt/TiO_2$ interface in the CO_2 reduction activity. Our simulation results qualitatively agree with the photocatalysis experiments.

METHODS

***Ab Initio* Calculations.** We performed the *ab initio* DFT calculations using VASP[54] and QE[55] on the AWS EC2 computing platform. As discussed, the MLIP was trained on VASP-generated data sets, and a few DFT calculations were performed and validated using QE simulations. We used a plane-wave basis set and a pseudopotential approach. For the exchange-correlation of electrons, we used the generalized-gradient approximation (GGA) in the form of the Perdew−Burke−Ernzerhof (PBE) functional.[56] We used the projector-augmented wave (PAW) pseudopotential method[57] for describing electron−ion interactions. Here, we chose rutile TiO_2(110) since it is the most stable among its various surfaces and the extensively studied model system.[31] We constructed 13-atom subnanometer-sized CuPt nanoclusters, denoted by $Cu_{(13-n)}Pt_n$. The motivation for the choice of magic-numbered clusters partly arises from several earlier computational studies, e.g., Refs. 58−62 and partly comes from the computationally tractable combinatorial problem. Further details on the DFT calculations, energetics calculations, and Bader charge analysis can be found in the Supporting Information.

Machine-Learning Interatomic Potential. To solve a combinatorial problem related to the complexities of structures involving five different chemical elements, we built a machine-learning model based on Allegro, a deep equivariant neural network architecture.[33] We used a 6 Å radial cutoff and 2 interaction blocks for the Allegro-based MLIP. A polynomial envelope with a cutoff of $p = 6$ and eight trainable Bessel functions were used for the basis expansion of the radial distances. We restricted the maximum irreducible representation of SO(3) for internal rotational features (i.e., the maximum order of geometric tensor embeddings transforming like type l spherical harmonics) to $lmax = 2$. For each l, we allowed both even and odd parity features. The two-body embeddings consist of 3 layers of dimensions (32, 64, 128). Within each interaction block, we used latent MLIPs consisting of 3 layers of dimensions (128, 128, 128). For nonlinear activations, sigmoid linear unit (SiLU) functions were used throughout the architecture. The MLIP optimizers, learning rates, and numerical precision are discussed in SI.

We employed an iterative training approach following the creation of an initial potential. Structures generated from BHMC simulations,[42,45] accelerated by the trained MLIP were screened through a workflow for identifying unique configurations (utilizing uniform manifold approximation and projection (UMAP) and K-means clustering). Single-point DFT calculations of configurations exhibiting high errors relative to the MLIP predictions were incorporated into the training set. Iterations persisted until convergence in terms of energy (<1 meV/atom) and force errors (<0.1 eV/Å) were achieved. Additional details regarding this method are provided in SI.

Sampling Unbiased Training. The MLIP training data set, previously described, encompasses the atomic coordinates,

https://doi.org/10.1021/acs.jpcc.4c02275
J. Phys. Chem. C 2024, 128, 14247−14258

Table 1. Sample Names, Input Compositions, and Final (Resulting) Compositions[a]

sample name	input composition (mol %)	final composition (mol %)
0Pt-0Cu	0% H_2PtCl_6 + 0% $Cu(NO_3)_2$	0% Pt + 0% Cu
0.14Pt-0.4Cu	0.14% H_2PtCl_6 + 1.25% $Cu(NO_3)_2$	0.14% Pt + 0.4% Cu
0.14Pt-0.6Cu	0.14% H_2PtCl_6 + 2.5% $Cu(NO_3)_2$	0.14% Pt + 0.6% Cu
0.5Pt-0.2Cu	0.5% H_2PtCl_6 + 0.5% $Cu(NO_3)_2$	0.5% Pt + 0.2% Cu
1.25Pt-0.4Cu	1.25% H_2PtCl_6 + 1.25% $Cu(NO_3)_2$	1.25% Pt + 0.4% Cu
1.79Pt-0Cu	1.79% H_2PtCl_6 + 0% $Cu(NO_3)_2$	1.79% Pt + 0% Cu

[a]The final compositions were measured by energy-dispersive X-ray spectroscopy (EDX).

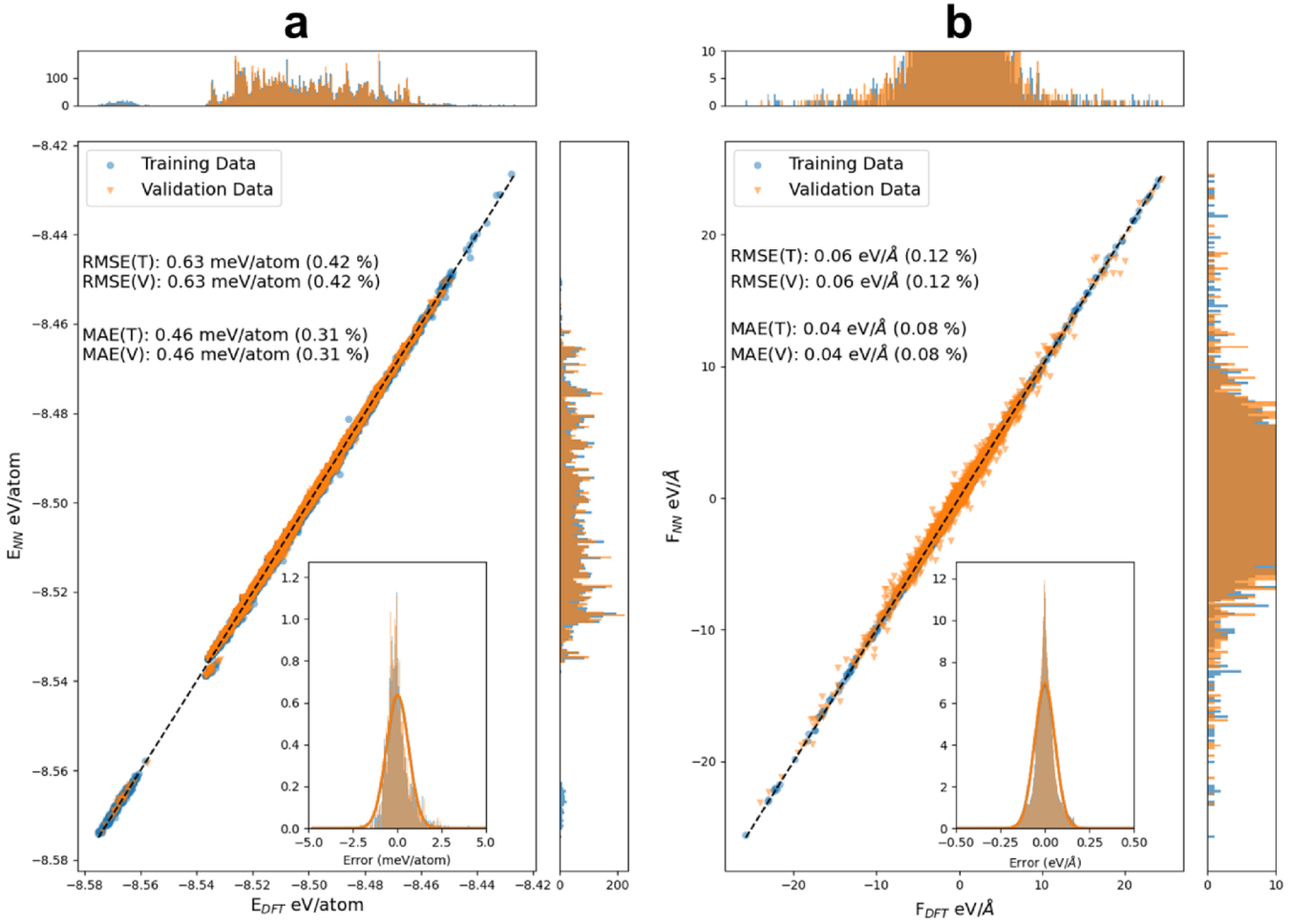

Figure 1. Parity plots showing the performance of MLIP for CO_2 adsorbed on $Cu_{(13-n)}Pt_n/TiO_2$ systems, $n = 0, \cdots, 13$, for (a) energies and (b) forces. The histograms in the margins show the corresponding distributions for the training and validation data. Insets: Distribution of prediction errors; solid lines indicate a fitted normal distribution.

energy, and forces of the CO_2@$Cu_{(13-n)}Pt_n/TiO_2$ systems. The (6×2)-$TiO_2(110)$ substrate, featuring a single oxygen vacancy, interacts with $Cu_{(13-n)}Pt_n$ nanoclusters ($n = 0-13$), and CO_2 is positioned at various adsorption sites. Overall, the training data includes $\sim 1.9 \times 10^6$ bulk atoms (TiO_2 substrate) and $\sim 0.73 \times 10^6$ surface atoms (consisting of 4690 C and O atoms from CO_2 and $\sim 0.12 \times 10^6$ Pt/Cu atoms). As a result, the MLIP training inherently favors TiO_2 atoms to reduce overall prediction errors for the predicted forces, sacrificing surface Ti and O atoms and the atoms comprising the nanoparticles and adsorbate, which are crucial for understanding surface science and catalytic activity.

This bias can be quantified by defining a Gaussian density function (GDF) for the encoding of an atomic environment that describes the radial and angular distributions (symmetry functions $\mathbf{G}$) of the neighboring atoms within a certain cutoff radius (see SI). For an arbitrary $\mathbf{G}$ for an atomic species in the entire space, we define the Gaussian density function $\rho(\mathbf{G})$ as

$$\rho(\mathbf{G}) = \frac{1}{M}\sum_{j=1}^{M} \exp\left(-\frac{1}{2\sigma^2}\frac{|\mathbf{G}-\mathbf{G}_j|^2}{D}\right) \quad (1)$$

where σ is the Gaussian width, D is the dimension of the symmetry function vector, and M is the total number of atoms in the entire data set. $\rho(\mathbf{G})$ ranges between 0 and 1, where $\rho(\mathbf{G}) \sim 0$ represents scarce training points and $\rho(\mathbf{G}) \sim 1$ represents abundant training points.

To address biases arising from the redundancy of atomic environments in the training set, we also acknowledge the

https://doi.org/10.1021/acs.jpcc.4c02275
J. Phys. Chem. C 2024, 128, 14247−14258

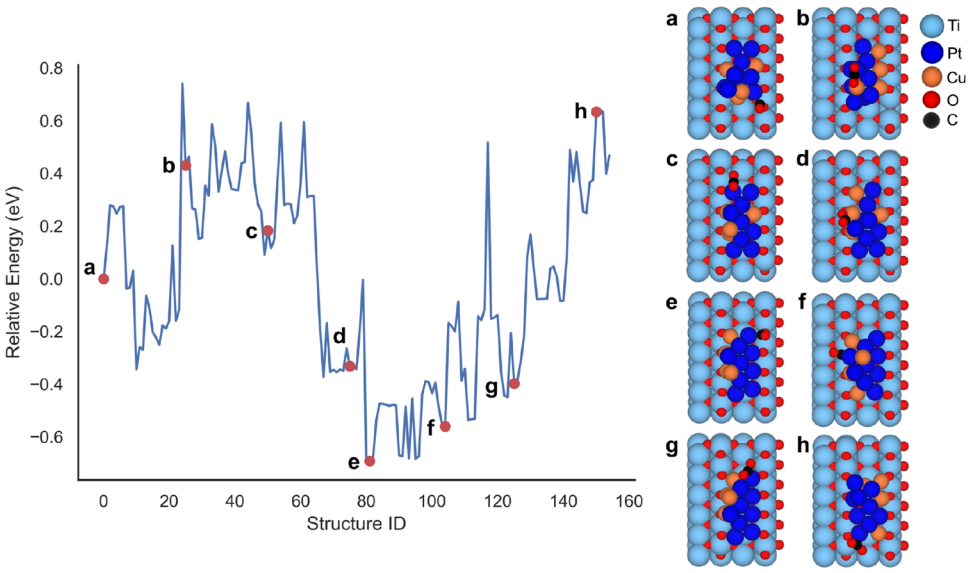

Figure 2. Exploration of structures of CO_2@$Cu_{(13-n)}Pt_n$ systems via modified basin-hoping Monte Carlo simulations, for example, $n = 9$. The relative energy (left) is given with respect to the energy of the initial seed configuration. The red dots represent the minimum of the potential energy surface. The corresponding structures are also shown (right, parts a−h). Configuration (e) has the lowest energy.

nonuniformity in training on atomic forces. The existing loss functions for MLIP training treat the absolute error in forces as constant irrespective of the force magnitude, leading to higher relative force errors for smaller values. To overcome the identified issues, we propose the use of an alternative weighted loss function in the MLIP model to ensure improved and uniform training for *ab initio* DFT data. The modified loss function takes the following form:

$$\Gamma = \frac{1}{N}\sum_{i=1}^{N}\left(\frac{E_i^{\mathrm{DFT}} - E_i^{\mathrm{NNP}}}{n_i}\right)^2 + \frac{\mu}{3M} \sum_{j=1}^{M}\left[\Theta\left[\frac{1}{\rho(\mathbf{G}_j)}\right] + Ae^{-|a\mathbf{F}_j^{\mathrm{DFT}}|}\right]|\mathbf{F}_j^{\mathrm{DFT}} - \mathbf{F}_j^{\mathrm{NNP}}|^4 \quad (2)$$

$$\Theta(x) = \frac{Bx}{1 + e^{-bx+c}} \quad (3)$$

where B is a scaling factor used to tune the impact of low-force data on the loss function (chosen to be 10 here), μ determines the relative weight of the force error with respect to the energy error in the loss function ($\mu = 1$ here), Θ is a monotonically increasing function (modified sigmoid function), A is a normalizing constant (the average of Θ is 1), and b and c are parameters that are fine-tuned for balanced training (chosen to be 150 and 1.0, respectively).

Experimental Details. *Synthesis of CuPt Nanoparticles Decorated with P25.* The sequential photodeposition of metal nanoparticles generally produces bimetallic nanoparticles due to the spontaneous accumulation of excited state electrons at metallic sites on the semiconductor surface.[13,63,64] Bimetallic CuPt nanoparticles supported on commercial TiO_2 (P25 by Evonik) were synthesized using the methods reported by Sorcar et al.[13] Before the synthesis of CuPt nanoparticles, reduced P25 was initially prepared by mixing 200 mg of P25 with 30 mg of $NaBH_4$ in a mortar and pestle. The powder was then heated under an inert atmosphere (Ar flow) at 350 °C for about an hour. Upon cooling, P25 was purified by washing with water and ethanol, and the sample was collected by centrifugation. This process was repeated at least five times until the solution's pH was neutral. The resulting powder was dried overnight in a vacuum oven at 100 °C. The platinum was deposited onto reduced P25 via photodeposition. 40 mg of P25 was initially dispersed in 10 mL of a 4:1 H_2O:CH_3OH solution. H_2PtCl_4 solution was then added to the dispersion and allowed to stir for 1 h. The dispersion was then irradiated by AM1.5 light with a 300 W Xe lamp at 1 sun intensity for 2 h. The resulting P25 decorated with Pt nanoparticles was washed with water and ethanol, collected by centrifuging, and dried under a vacuum. Copper was subsequently deposited using a similar method with $Cu(NO_3)_2$ instead of H_2PtCl_4. The Cu and Pt input compositions are summarized in Table 1, along with the resulting final compositions determined by energy-dispersive X-ray spectroscopy (EDX). The CuPt-P25 samples were then deposited onto glass frits before loading them into the photoreactor. Dispersions of the samples in isopropanol were drop-coated onto AceGlass glass frits with porosity C until about 15 mg was loaded. The frits were then dried overnight under a vacuum.

Experimental Setup for Measuring the Photocatalytic Activity of CuPt-P25. The catalyst-coated glass frit was then placed in a custom-built steel photoreactor fitted with a quartz window. Before testing, the reactor was purged by evacuating it and refilling it with 1:1 Ar:CO_2 ten times. Ar (1.5 sccm) and CO_2 (1.5 sccm) were bubbled through a water-filled gas washing bottle and fed into the reactor from the top, passing through the frit, and exiting the bottom of the reactor. The reactor was then irradiated by a 300 W Xe lamp at 1 sun intensity through an AM1.5 filter. The product gas composition was analyzed using gas chromatography (SRI GC MG5).

RESULTS

MLIP Training and Validation. In Figure 1, we show the parity plot of MLIP predicted against the DFT-calculated energy and forces along with the distribution of errors (inset). For the training set (8646 structures), the root-mean-squared error (RMSE) and mean-absolute error (MAE) in energy are 0.63 and 0.46 meV/atom, respectively, while those in forces are 0.06 and

https://doi.org/10.1021/acs.jpcc.4c02275
J. Phys. Chem. C 2024, 128, 14247−14258

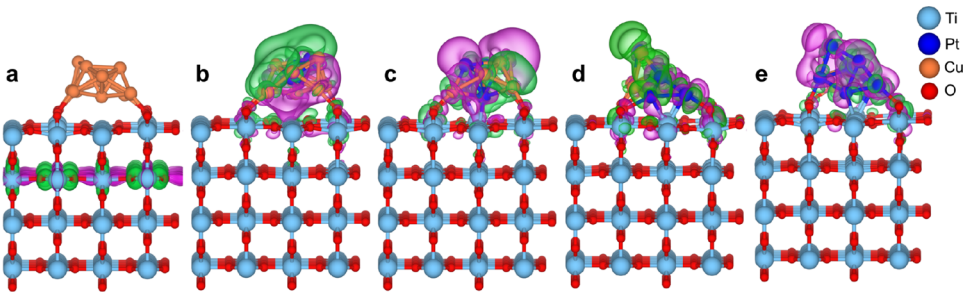

Figure 3. Spatial localization of frontier electronic states corresponding to the topmost valence band calculated at the Brillouin zone center of the $Cu_{(13-n)}Pt_n/TiO_2$ systems for n equal to (a) 0, (b) 3, (c) 5, (d) 9, and (e) 11. The green and pink iso-surfaces represent the partial electron densities of $+10^{-4}\ e/a_0^3$ and $-10^{-4}\ e/a_0^3$, respectively, where a_0 is the Bohr radius.

0.04 eV/Å, respectively. The model is also tested using a validation set (9633), which resulted in equivalent RMSE and MAE errors.

To obtain a better understanding of MLIP errors in learning *ab initio* data, we obtained decomposed-force parities for CO_2, the CuPt cluster, and TiO_2 (Figure S3). Even with less representation in the overall training data, the force prediction errors for both CO_2 and the nanocluster are comparable to the overall RMSE of the force distribution (Figure S3). The effect of weighted training is discussed further in the Supporting Information (Figure S4).

The generation of the initial training data set is important for the MLIP model development. The utilization of the MLIP model together with the BHMC then allows us to explore the global PES of atomic systems, including various effects such as changes of the position of surface oxygen vacancies on $TiO_2(110)$, the position of nanocluster atoms, CO_2 adsorption sites, and the shape of the supported nanoclusters. The use of the DFT approach for this task is computationally expensive; however, incorporating MLIP trained on limited data offers a more efficient alternative. Below, we describe the PES of CO_2 adsorption explored by our developed MLIP model using the BHMC approach.

Potential Energy Surface Exploration for Adsorption of CO_2 on CuPt/TiO_2. We perform BHMC+MLIP simulations to efficiently determine the low-energy configurations of CO_2@ $Cu_{(13-n)}Pt_n/TiO_2$. Analyzing the relative energy of CO_2@ $Cu_{(13-n)}Pt_n/TiO_2$, e.g., n = 9 (Figure 2), the BHMC-explored PES curve reveals that the initially explored structures (b−c) are higher in energy, which evolves toward minimum region structures (e−f). If lower-energy structures are not found, then the algorithm gradually accepts higher-energy configurations, moving to higher-energy basins (g−h).

This exploration yields the lowest energy basins with a common feature, i.e., CO_2 adsorption occurs at the CuPt/TiO_2 interface. We performed similar simulations with different Cu/Pt cluster compositions and discussed the minimum CO_2 adsorption structures. We provide details of the exploration procedure in the Supporting Information. Despite MLIP's low validation errors, comparing the structural stability within a small energy range is not viable. We adopt a 0.1 eV energy window, adding BHMC-generated structures with energy differences less than 0.1 eV to the low-energy ensemble. Subsequently, DFT relaxation is applied to this ensemble to eliminate potentially small MLIP errors.

The extremely large configurational space is apparent from an illustration of PES exploration for a model system (Figure 2), whose configurations are found to be different cluster shapes with various arrangements of Pt/Cu atoms. There are several possible adsorption sites for CO_2, including the CuPt/TiO_2 interfacial sites and different oxygen vacancy sites on $TiO_2(110)$.

Interaction of CuPt Nanoclusters with TiO_2. For the CuPt composition, the cluster−support interaction is facilitated mostly by chemical bonds formed between Cu and bridging O atoms and bonds between Pt and bridging O and/or 5-fold (5*f*)-coordinated Ti atoms. The distributions of the Cu−O bond lengths (Figure S5) for the lowest-energy configurations and more details can be found in SI. Owing to the metal−support interactions, the $Cu_{(13-n)}Pt_n$ cluster adopts a hemispherical shape (Figure 3). Regardless of the composition, the supported CuPt clusters prefer a 3D geometrical shape.

It is important to understand the distribution of CuPt/TiO_2 frontier states (fully occupied) since the states spatially distributed around the interfacial atoms would play an important role in ultrafast dynamics and thereby photoinduced reactions.[65] In Figure 3, we show the fully occupied states for some compositions of $Cu_{(13-n)}Pt_n/TiO_2$, n = 0, 3, 5, 9, and 11. As shown, the frontier states are spatially localized at the interface and around the Cu−Pt atoms when n = 3, 5, and 9. Although the spatial localization is found to vary with Cu−Pt composition, the common feature is that there is some distribution of the maximum valence band (VB) frontier states. In contrast, the Cu_{13}/TiO_2 VB frontier states are localized at the TiO_2 second layer (from the top). The other calculated states for the Cu_{13}/TiO_2 system are shown in Figure S6. These results suggest that the CuPt/TiO_2 interface was more active than the Cu/TiO_2 interface.

CO_2 Interaction with CuPt/TiO_2. We now examine the interaction of CO_2 with $Cu_{(13-n)}Pt_n/TiO_2$ via DFT by considering the lowest-minimum configurations predicted by MLIP+BHMC simulations. For all CuPt compositions, we find that CO_2 adsorption is thermodynamically favorable, and CO_2 is activated (Table 2). Regardless of the CuPt composition, CO_2 is adsorbed at the interface, and the degree of interaction depends on the composition and shape of the clusters. This interaction of CO_2 with Pt_{13}/TiO_2 is stronger than that with the Cu_{13}/TiO_2 systems. Although we do not observe any specific trend in the adsorption energies, our calculations suggest that the magnitude of the CO_2 interaction would be higher for CuPt clusters than for pure Cu. Compared to the bond length (1.162 Å) and angle (180°) of CO_2 in the gas phase, the C−O bond elongates upon its adsorption, and the bond angle changes to 121−134°. Taken together, the results of the CO_2 interaction with the CuPt/TiO_2 systems with various Pt/Cu compositions (E_{ads} = −0.50 to −1.2 eV), the charge transfer to an adsorbed CO_2 (∼0.7*e* to 0.9*e*) and the elongation of the C−O bond (∼0.2 Å) and the substantial

https://doi.org/10.1021/acs.jpcc.4c02275
J. Phys. Chem. C 2024, 128, 14247−14258

Table 2. Adsorption and Activation of CO_2 at the Interface of $Cu_{(13-n)}Pt_n/TiO_2(110)$, n = 0, ···, and 13, in the Lowest-Energy Configurations[a]

Pt_n	adsorption site	E_{ads}	$d_{(CO)}$	∠OCO	$d_{(C-Cu)}$ $d_{(C-Pt)}$	charge gained by CO_2
0	Cu & O_{vac}	−0.42	1.266, 1.321	121.4	1.940	1.00
1	Cu & O_{vac}	−0.62	1.212, 1.370	122.9	1.921	0.87
2	Pt & O_{vac}	−1.24	1.271, 1.306	121.3	2.006	0.95
3	Pt & O_{vac}	−0.71	1.218, 1.320	127.7	2.028	0.78
4	Pt & O_{vac}	−0.67	1.217, 1.315	128.3	2.020	0.75
5	Pt & O_{vac}	−0.95	1.253, 1.287	125.5	1.997	0.79
6	Pt & O_{vac}	−0.80	1.216, 1.352	124.1	2.021	0.80
7	Pt & 5*f* Ti	−0.86	1.246, 1.251	134.6	1.977	0.54
8	Pt & O_{vac}	−0.94	1.216, 1.364	123.0	2.020	0.82
9	Pt & O_{vac}	−1.15	1.232, 1.358	122.5	1.987	0.96
10	Pt & 5*f* Ti	−0.48	1.217, 1.309	128.2	2.016	0.64
11	Pt & O_{vac}	−0.67	1.215, 1.350	124.6	2.017	0.79
12	Pt & 5*f* Ti	−1.03	1.240, 1.265	133.6	1.961	0.53
13	Pt & 5*f* Ti	−1.01	1.242, 1.266	134.4	1.951	0.58

[a]Given are the adsorption sites, adsorption energy E_{ads} (eV), CO bond length $d_{(CO)}$ (Å), the ∠OCO of the OCO bond angle (deg), the distance between C and Cu or Pt (Å), and the net charge (e) gained by adsorbed CO_2 according to Bader decomposition of the charge density (the details of the method is given in SI). The $d_{(CO)}$ and ∠OCO of the gas-phase CO_2 are, respectively, 1.162 Å and 180°.

reduction of ∠OCO (55−59°), we show that CuPt/TiO_2 systems facilitate CO_2 activation.

Figures 4 and S7 (see SI) present the lowest-minimum structures of the CO_2@$Cu_{(13-n)}Pt_n/TiO_2$ configurations. CO_2 adsorbs at the interface of Cu_{13}/TiO_2 such that C attaches to a Cu atom and the $O_{(CO_2)}$ atom fills the O vacancy sites (Figure 4a). For $Cu_{(13-n)}Pt_n$ with $n \neq 7, 10, 12, 13$ ($n > 0$), CO_2 adsorbs at the interface with an $O_{(CO_2)}$ atom occupying an O vacancy site and C bonded to Pt, thus preferring Pt over a Cu site (Figure 4b−e). For n = 13, CO_2 adsorbs such that C is bonded to Pt and $O_{(CO_2)}$ to 5*f* Ti (Figure 4f). The CO_2 adsorption geometries for = 7, 10, and 12 are similar to those of n = 13. These results indicate that the CuPt/TiO_2 interface serves as active sites for CO_2 adsorption, particularly highlighting the importance of interfacial Cu/Pt and surface Ti atoms (near O vacancies).

The electron density difference ($\Delta\rho$) plot (Figure 4g) shows that the resulting electron density is redistributed in the bonding regions of the *CO_2 atoms (C, O_1, O_2) and interfacial atoms (Pt/Ti). Thus, the favorable interaction between CO_2 and Cu_4Pt_9/TiO_2 is mediated by the interface. The charge redistribution, upon CO_2 interaction with Cu_4Pt_9/TiO_2, suggests that the charge transfer takes place between the two subsystems. Charge accumulation occurs around the $O_{(CO_2)}$ atoms and charge depletion occurs around a C atom and surface Ti atoms. Some charge additions to the *CO_2 antibonding state

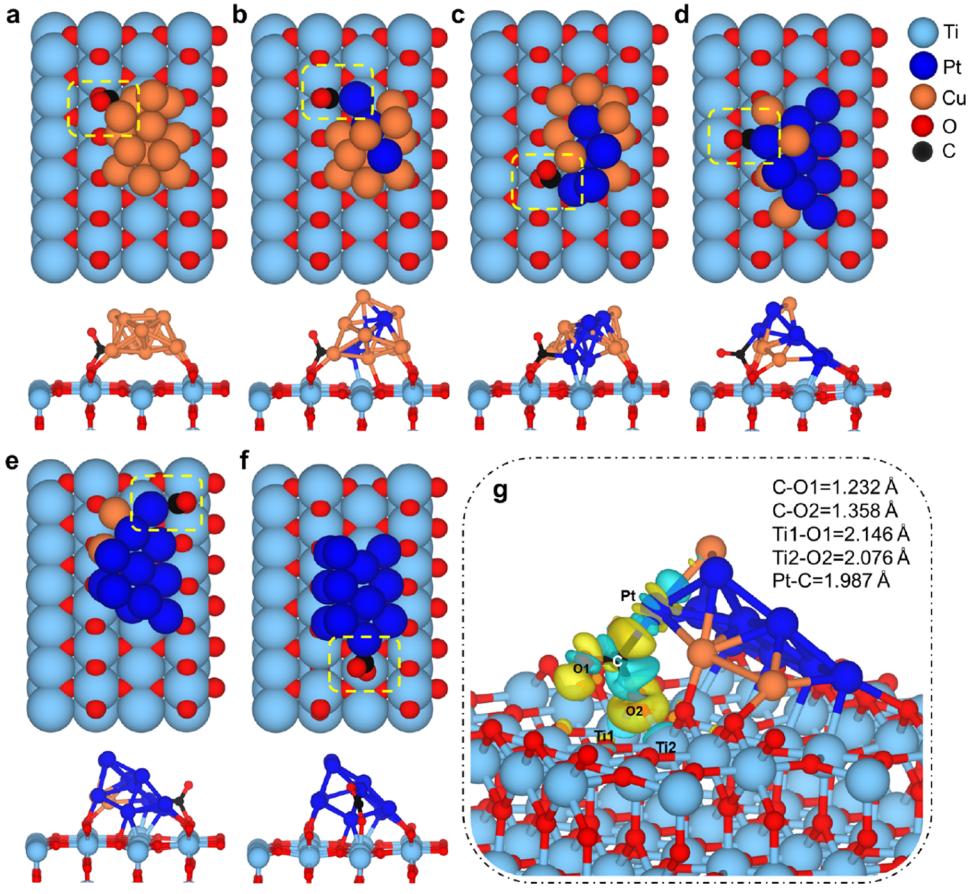

Figure 4. Schematic representation of DFT-optimized structures of adsorbed CO_2 (dashed yellow boxes) on $Cu_{(13-n)}Pt_n/TiO_2(110)$ for n equal to (a) 0, (b) 3, (c) 5, (d) 9, (e) 11, and (f) 13 (top and side views). In (a−e), the O atom of *CO_2 fills a surface O vacancy, and in (f) an *CO_2 O bond to a 5-fold-coordinated Ti atom. (g) Electron density difference for configuration (d). The yellow and cyan regions represent the positive and negative isosurfaces with electron densities of +0.005 e/a_0^3 and −0.005 e/a_0^3, respectively (a_0 is the Bohr radius).

https://doi.org/10.1021/acs.jpcc.4c02275
J. Phys. Chem. C 2024, 128, 14247−14258

can trigger C−O bond elongation. Indeed, based on the partial charge analysis, a net charge transfer of 0.96e takes place from Cu_4Pt_9/TiO_2 to adsorbed CO_2 (Table 2), inducing C−O bond elongation and thereby facilitating CO_2 activation.

Stability of CO. The stability of *CO is important for the reaction pathway for the formation of CH_4. Now, we examine *CO stability by calculating the adsorption energies and geometries. First, we consider pristine $Cu_{(13-n)}Pt_n/TiO_2(110)$ systems, $n = 0-13$, starting with the initial configurations of CO at/near nanocluster sites, where the C atom of the adsorbed CO_2 is attached (in $*CO_2$ configurations) and one oxygen (from CO_2) is attached to an oxygen vacancy. We relax the geometry of each configuration. After full relaxation, we remove CO from the $*CO@Cu_{(13-n)}Pt_n/TiO_2$ system and then relax isolated CO and $CuPt/TiO_2$ individually. We then calculate the adsorption energy (E_{ads}), as described in the Methods section in the Supporting Information. CO adsorption on each TiO_2-supported CuPt cluster is found to be stronger than that on the supported Cu_{13}. When $n = 1$, CO is adsorbed at a Cu−Pt bridge site. In all other Cu−Pt compositions, including pure Pt, CO is preferentially adsorbed at the Pt top site. For Cu_4Pt_9, the CO adsorption energy is ∼ −2.5 eV, which supports our model choice for exploring the other elementary steps. While the CO adsorption is less strong on pure Cu_{13}, it is very strong on pure Pt_{13}. Therefore, our results suggest that suitable CuPt compositions may be suitable for binding *CO. These calculations suggest that the TiO_2-supported CuPt clusters better stabilized *CO than Cu clusters. Second, we consider $Cu_{(13-n)}Pt_n/TiO_2(110)$ systems with a single oxygen vacancy. In this case, the shapes of the supported nanoclusters are slightly different from those of the $Cu_{(13-n)}Pt_n/TiO_2(110)$ systems with CO_2 adsorbate. The calculated geometries are shown in Figure S8. The adsorption energies and geometric parameters are listed in Table 3. For completeness, we also provide the calculated adsorption geometries and energies of CO adsorbed on $Cu_{(13-n)}Pt_n$ nanoclusters supported on $TiO_2(110)$ with a single oxygen vacancy in the Supporting Information (Figure S9 and Table S1).

Table 3. Adsorption of CO on $Cu_{(13-n)}Pt_n/TiO_2(110)$, $n = 0$, ···, and 13, in Lowest-Energy Configurations[a]

Pt_n	adsorption site	E_{ads}	$d_{(CO)}$	$d_{(C-Cu)}$	$d_{(C-Pt)}$
0	Cu	−1.20	1.151	1.829	0.000
1	Cu & Pt	−1.91	1.182	1.981	1.918
2	Pt	−1.24	1.162	3.359	1.867
3	Pt	−1.57	1.192	2.744	1.931
4	Pt	−1.80	1.197	2.480	1.929
5	Pt	−2.26	1.190	3.672	1.928
6	Pt	−1.84	1.163	2.958	1.843
7	Pt	−1.91	1.163	3.197	1.864
8	Pt	−1.49	1.162	3.008	1.864
9	Pt	−2.50	1.167	2.877	1.840
10	Pt	−2.95	1.162	3.773	1.822
11	Pt	−1.59	1.163	3.212	1.847
12	Pt	−2.78	1.167	3.362	1.822
13	Pt	−2.74	1.167	0.000	1.823

[a]Given are the adsorption sites, adsorption energy E_{ads} (eV), CO bond length $d_{(CO)}$ (Å), and the shortest distance between C and Cu or Pt (Å).

Structures and Energetics of the Intermediates. We now present the results for the structural and energetic properties of the Cu_4Pt_9/TiO_2 model system when interacting with the reactants (CO_2/H_2O) and key intermediates of CO_2 reduction. Figure 5 shows the energy profile for the reaction between CO_2 and H_2O (reactants) and some key intermediates adsorbed on Cu_4Pt_9/TiO_2. The relative energies of all adsorbed species (with or without coadsorption) are given in reference to the sum of the energies of gas-phase $CO_{2(g)}$ and $H_2O_{(g)}$, and of Cu_4Pt_9/TiO_2. The reaction energy (ΔE) is the difference in the energy between the initial and final states. The adsorption of H_2O in the presence of $*CO_2$ is favorable ($\Delta E = -0.79$ eV). H_2O adsorbs at the Ti site with H being closer to a bridging O atom. $TiO_2(110)$ has been well studied for H_2O activation.[6,9,49,66,67] CO_2 adsorption is energetically favorable ($\Delta E = -1.15$ eV). Based on CO_2 activation, we are mainly interested in the chemical activity at/near the interface.

Once *CHOO is formed via hydrogenation, i.e., $*CO_2 + *H \rightarrow *CHOO + *$ ($\Delta E = +0.60$ eV), it can undergo self-dissociation to *CHO and *O (Figure 5) with an increase of energy ($\Delta E = -0.21$ eV). Similarly, $*CO_2 + *H \rightarrow *COOH + *$ is endothermic ($\Delta E = +0.27$ eV). Although these steps require some energy, the reactions may be activated under normal reaction conditions. The calculated energetics provide some indication that while *CO formation from CO_2 dissociation is a favorable process (*CO hydrogenation can proceed to yield *CHO formation, being more thermodynamically favorable than *COH formation.[68]), $*CO_2$ hydrogenation might also be feasible under an external driving force. As an alternative pathway, $*CO_2$ dissociation occurs with *CO formation. $*CO_2$ dissociation in coadsorption with *H at a bridging O atom is more exothermic ($\Delta E = -0.62$ eV) than $*CO_2$ dissociation with *H at a Cu−Pt site ($\Delta E = -0.35$ eV).

Both $*CO_2$ and *CO, as well as the stabilities of other intermediates such as *CH, $*CH_2$, and $*CH_3$, are important for the selectivity of $CH_{4(g)}$ over CO(g). Now, we examine the structure and energetics of $*CH_2OH$ (which can be formed via the reaction between *H and $*CH_2O$, which can be formed either by $*CH_2OO$ dissociation[27] or by an *H + *CHO step).[27,69] CH_2OH adsorbs at the interfacial sites, where C attaches to Pt (2.034 Å) and the OH functional group occupies an O-vacancy site (Figure 6a). The dissociation step $*CH_2OH + * \rightarrow *CH_2 + *OH$ on Cu_4Pt_9/TiO_2 is thermodynamically more favorable ($\Delta E = -0.65$) than on Pt/TiO_2 ($\Delta E = -0.12$ eV[27]) and on Cu/TiO_2 ($\Delta E = 0.21$ eV[70]), thus indicating that $*CH_2$ formation is thermodynamically feasible and $*CH_2$ is stabilized by interfacial Cu and Pt atoms, which can serve as active sites for $*CH_2$ formation and other relevant reactions. The activation energy for this reaction step on Cu_4Pt_9/TiO_2 is 0.19 eV, thus suggesting that the formation of $*CH_2$ might be kinetically favorable. These results suggest that CuPt nanoclusters can provide a larger thermodynamic driving force for $*CH_2$ production via C−O bond breaking than Pt or Cu clusters. Since the Pt−H distance (H of *OH) is only 2.322 Å, the Pt site can facilitate the reaction between $*CH_2$ and *OH to form $*CH_3$ and $*O^{ad}_{vac}$. For the feasibility of this process, however, *OH bond scission and additional C−H bond formation should occur simultaneously. The resulting $*CH_3$ then reacts with *H to form $*CH_4$ or $CH_{4(g)}$ (Figure S11). The $*CH_3 + *H \rightarrow * + * + CH_{4(g)}$ step is feasible at room temperature. The CH_3 formation route might proceed with the formation of *CH, which reacts with *H to form $*CH_2$, which then subsequently reacts with *H to form $*CH_3$. Indeed, the formation of *CH from the dissociation of *CHOH, which is also activated at the

https://doi.org/10.1021/acs.jpcc.4c02275
J. Phys. Chem. C 2024, 128, 14247−14258

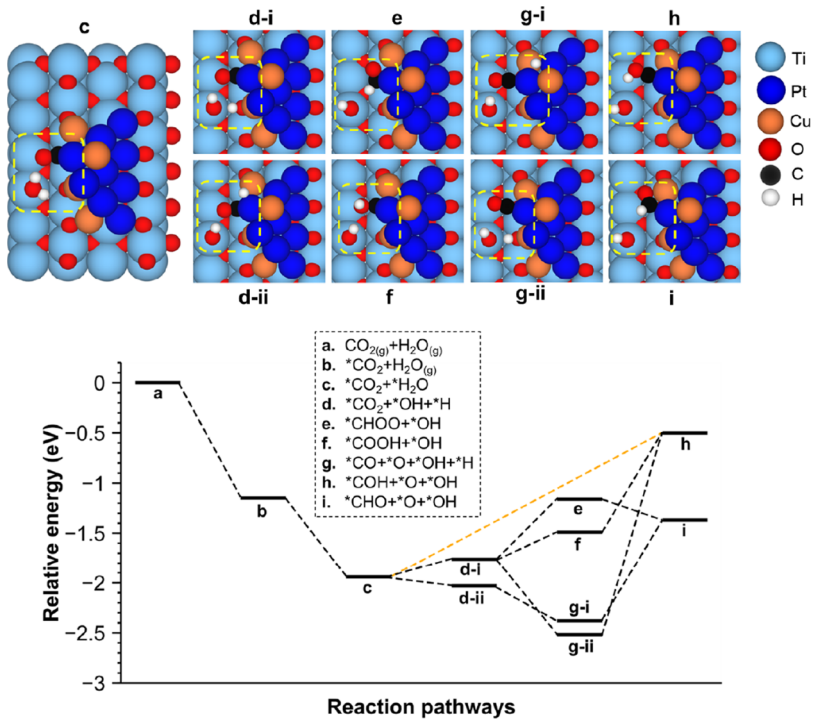

Figure 5. Energy profile for the elementary reaction steps involving reactants ($CO_{2(g)}$, $H_2O_{(g)}$), CO_2 activation, and catalytic CO_2 conversion to intermediates: (a) $CO_{2(g)} + H_2O_{(g)}$, (b) $*CO_2 + H_2O_{(g)}$, (c) $*CO_2 + H_2O*$, and (d) $*CO_2 + *OH + *H$ where *H is adsorbed at a bridging O atom (d-i) and at the Cu−Pt site (d-ii), (e) *CHOO + *OH, (f) *COOH + *OH, and (g) $*CO + *O^{ad}_{vac} + *OH + *H$, where *H is adsorbed at the Cu−Pt site (g-i) and at a bridging O atom (g-ii), (h) $*COH + *O^{ad}_{vac} + *OH$, and (i) $*CHO + *O^{ad}_{vac} + *OH$. Here, $*O^{ad}_{vac}$ (labeled as *O in the inset) refers to the adsorbed oxygen atom filling the surface O vacancy sites. The top panel shows top views of the atomic configurations (side views are provided in Figure S10). The dashed yellow boxes highlight adsorbed species with energetically preferred sites.

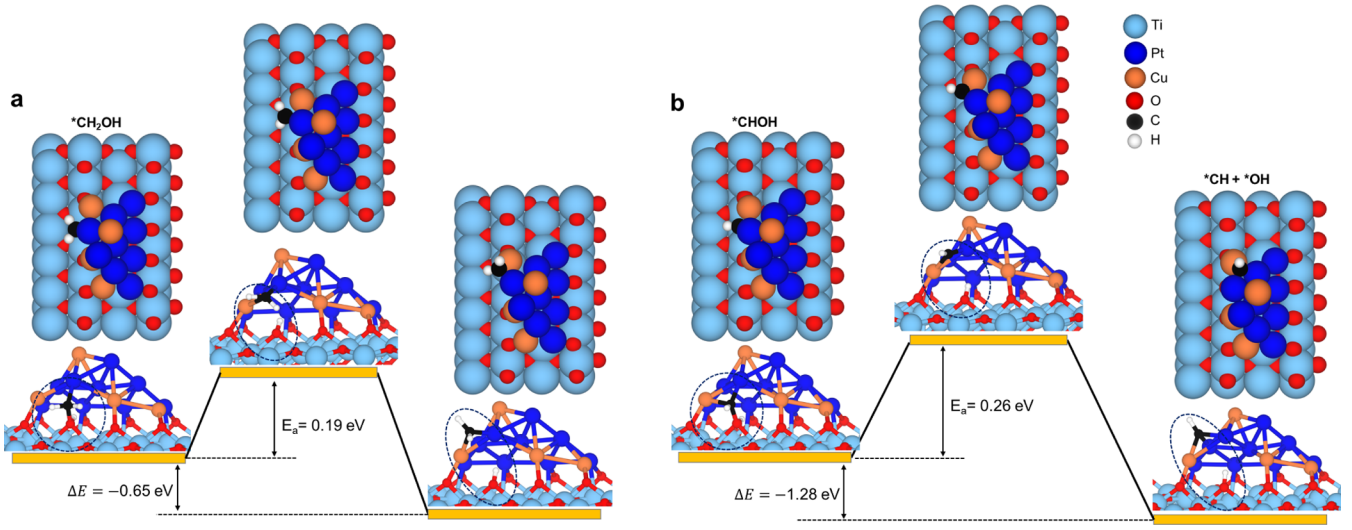

Figure 6. Reaction energetics of (a) dissociation of $*CH_2OH$ into $*CH_2$ and *OH and (b) *CHOH into *CH and *OH on Cu_4Pt_9/TiO_2. In both (a) and (b), the left, middle, and right panels show the initial, transition, and final states, respectively. In the dissociated phase of CH_2OH, CH_2 adsorbs at the bridge site of interfacial Cu and Pt atoms with bonding of C to Cu−Pt atoms, and OH fills the O vacancy site with the bonding of *OH oxygen with under-coordinated Ti atoms (compared to 5-fold-coordinated Ti). In the CHOH dissociated phase, CH adsorbs at a 3-fold site of interfacial Cu and two Pt atoms, whereas OH occupies the O vacancy site. Both reaction steps are energetically favorable with negative ΔE. The top and bottom panels represent the top and side views, respectively (the latter is rotated slightly for better visibility).

interface, is energetically favorable (ΔE = −1.28 eV), with an activation energy of 0.26 eV (Figure 6b).

Experimental Rationalization of CO_2 Photoconversion. We characterize the morphology and composition of the reduced P25 samples by scanning electron microscopy (Figure 7a) and EDX (Figure S12), respectively. The reduced P25 is irregular, with a particle size of <50 nm. We observe some high-contrast features after the photodeposition of Pt and Cu, indicating the formation of metal nanoparticles. The Pt detected by EDX is similar to the input Pt amount; however, the Cu detected is significantly less than the input Cu amount with 0.14Pt-0.6Cu and 1.26Pt-0.4Cu, which required ~2.5 and 1.25%

https://doi.org/10.1021/acs.jpcc.4c02275
J. Phys. Chem. C 2024, 128, 14247−14258

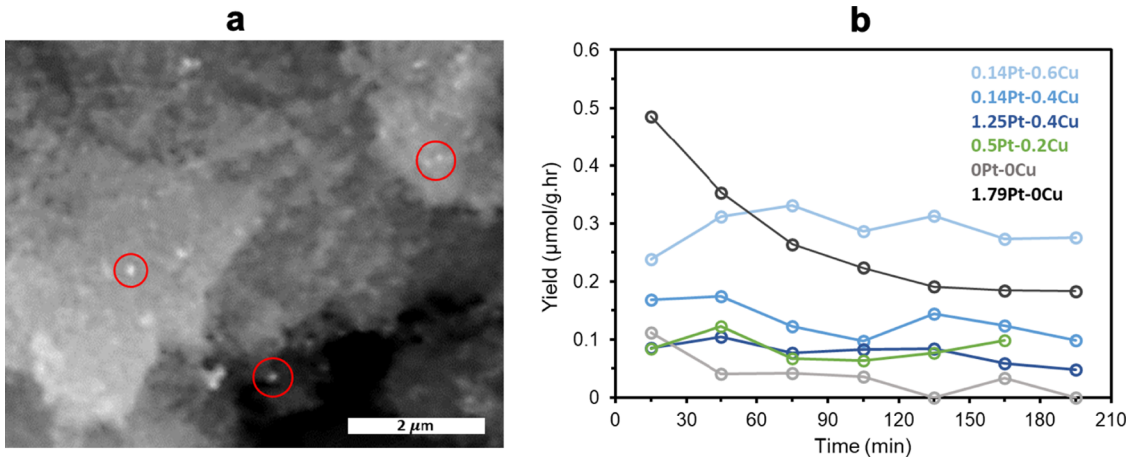

Figure 7. Morphology and photocatalytic activity of CuPt/P25 samples. (a) Scanning electron microscopy (SEM) micrograph of 1.25Pt-0.4Cu (in mol %) with the red circles highlighting some areas of high contrast likely associated with high Pt/Cu content. (b) CH_4 production of reduced P25 decorated with CuPt nanoparticles of various compositions (in mol %) of Pt and Cu added by photodeposition.

Cu, respectively. This incomplete photodeposition of Cu compared to that of Pt might be attributed to the lower reduction potential of Cu^{2+} than that of Pt^{2+} and the redox nature of Cu.

We perform photocatalytic reactor measurements under a humidified CO_2 and Ar flow, illuminated by an AM1.5 filtered Xe lamp focused to a 5 sun intensity. Figure 7b shows the CH_4 yield over time of photocatalytic reactions on CuPt/P25 samples at various CuPt compositions. The sustained CH_4 production is the highest for 0.14Pt−0.6Cu (with the photodeposition of 0.14 mol % Pt and 2.5 mol % Cu onto the reduced P25), in agreement with an earlier study by Sorcar et al.[13] The low Pt and high Cu composition produce a higher CH_4 yield. The CH_4 yield was initially higher for the 1.79Pt−0Cu samples, but it became deactivated over time. P25 samples with only Cu or Pt deposited or just reduced P25 alone produced significantly less CH_4, suggesting that the higher CH_4 yield is the consequence of the synergistic effects of Cu, Pt, and P25. The CO_2 photoconversion activity decreases substantially as both Pt and Cu loadings are increased, which is attributed to the growth of large-sized CuPt particles and the reduction of the interfacial density of Cu/Pt−TiO_2 sites, suggesting that the TiO_2−Pt/Cu interface is highly preferable for achieving higher photocatalytic conversion of CO_2 to hydrocarbons.

DISCUSSION

Compared to oxide supports[21,23] and metal surfaces,[71,72] CO_2 is chemically well activated by metal/oxide interfaces. From our DFT simulations, the defect-laden TiO_2(110) does not facilitate CO_2 activation (E_{ads} ∼ −0.2 eV, $d_{(C-O)}$ = 1.182 Å, and ∠OCO = 179.7°). Our simulation is thus consistent with the previous experimental measurements of the onset temperature for CO_2 desorption (∼175 K).[71] Since TiO_2 itself does not stabilize CO_2,[71] CO_2 reduction is not feasible. On well-defined metal surfaces, CO_2 adsorption is also weak, e.g., E_{ads} = ∼ 0.21−0.28 eV for Cu[73] and E_{ads} = ∼ 0.03 eV for Pt[74], and thus limits to trivial charge transfer between CO_2 and Cu/Pt catalysts. Because of the weak interaction with E_{ads} = −0.29 eV,[74] it can also desorb before its reaction with H.[27] The coupled systems of both Cu and Pt supported on TiO_2 can enhance CO_2 adsorption. While Pt_{25}/TiO_2(110) binds CO_2 with E_{ads} = −0.61 eV,[27] Cu_{10}/TiO_2(110) binds with E_{ads} = −0.65 eV.[75] Compared to bare TiO_2 or Cu/TiO_2, CuPt/TiO_2 can be considered a better catalyst owing to (1) higher $*CO_2$ stability at the interface and (2) interfacial Cu and Pt atoms providing sites for nucleophilic and electrophilic adsorbates.

For the catalytic conversion of CO_2 into hydrocarbons, atomic hydrogens (from the H_2O-splitting process) are required to be present on the catalyst surfaces so that they can react directly with either the $*CO_2$ reactant or *CO/*C to form CH-containing intermediates. The CuPt/TiO_2 interface provides active sites for the formation of the intermediates *CO, *CHOO, *CHO, $*CH_2OH$, *CH, $*CH_2$, and $*CH_3$, thus highlighting the importance of interfacial sites in the chemical activity of CuPt/TiO_2 systems for CO_2 conversion to hydrocarbons.

We propose the following reaction pathway: CO_2 adsorbs at the CuPt/TiO_2 interface with CO_2 oxygen at a vacancy site, and H_2O adsorbs at the 5*f* Ti site of the reduced P25, thus facilitating the formation of *H* and *CO at the interfacial Pt sites and leaving behind a surface of O^{2-}. Then, they can react to form intermediates required for the CH_4 formation pathway. Finally, the O-vacancy generation is assisted by the redox activity of the CuPt nanoparticles with some fractions of Cu on their surface.

Although MLIP/DFT simulations and experimental observations cannot be directly matched, our studies together can provide meaningful insights into the CuPt/TiO_2 photocatalytic systems. Although the model cluster size is much smaller than the experimental nanoparticle size, the results from the simulations of the TiO_2-supported model CuPt clusters with and without adsorbates have provided insights into the active sites at the interface and how the bimetallic particles and oxygen vacancies play an important role in CO_2 activation. The excellent chemical activity of CuPt/TiO_2 can be correlated with the thermodynamically favorable, moderate-to-strong interaction (E_{ads} = −0.67 to −1.24 eV) with CO_2 and the net charge gained by CO_2 (∼0.7−1.0*e*). The synergistic effect of the surface TiO_2, Cu, and Pt atoms at the interface results in stronger CO_2 adsorption with E_{ads} = −0.67 to −1.24 eV, charge transfer of ∼0.7−1.0*e* to $*CO_2$, CO_2 bond elongation, and change in ∠OCO to 121−134°, indicating CO_2 activation. For a $Cu_{11}Pt_2$ cluster, which is approximately equivalent to the experimental composition of 0.14Pt−0.6Cu, CO_2 is adsorbed at both the O vacancy and Pt sites. It is notable that CO_2 strongly interacts with $Cu_{11}Pt_2/TiO_2$ (E_{ads} ∼ −1.2 eV) together with C−O bond elongation of ∼0.2 Å, ∠OCO change to ∼121°, and

https://doi.org/10.1021/acs.jpcc.4c02275
J. Phys. Chem. C 2024, 128, 14247−14258

~0.9*e* gained by $*CO_2$, thus promoting CO_2 activation. Our examination for CO adsorption (without coadsorption) suggests that *CO stabilizes at the Pt site of $Cu_{11}Pt_2$, with adsorption energies of −1.24 eV (pristine) and −1.82 eV (defective). For the Cu_8Pt_5 and Cu_4Pt_9 compositions, CO adsorption (at the Pt site) is relatively stronger than that on $Cu_{11}Pt_2$ (see Tables 3 and S1). Thus, these results suggest that the catalytic activity of TiO_2-supported CuPt nanoclusters is dependent on the compositions of Cu and Pt. For higher Pt concentrations, selectivity for CH_4 was observed but with a lower yield. The activation of CO_2 at the CuPt/TiO_2 interface, along with the stability of *CO at the interfacial Pt atoms, could potentially enhance the reaction pathways, leading to the formation of CH_4, as evidenced by experimental observations.

CONCLUSIONS

In summary, using unbiased MLIP + BHMC together with *ab initio* DFT approaches, we demonstrate that $Cu_{(13-n)}Pt_n/TiO_2$ systems strongly facilitate the activation of CO_2 at the interfacial sites. The process is facilitated by charge transfer and direct interactions. The calculated CO_2 adsorption energies are from −0.5 eV to −1.2 eV, depending on the Cu/Pt ratio. The VB-maximum frontier states are spatially localized at the interfacial atoms, suggesting that these atoms are active sites for chemical reactivity.

The interface plays a key role in influencing the chemical activity of the CuPt/TiO_2 systems. The $*CO_2 + * \rightarrow *CO + *O$ step, in which oxygen fills the vacancy site and CO adsorbs at an interfacial Pt site, is energetically favorable. Other elementary steps can result in *CHOO, *CHO, $*CH_2OH$, *CHOH, *CH, and $*CH_2$ intermediates. The interface, with an optimal CuPt composition, bolsters the stability of *CO, suggesting higher activity and CH_4 selectivity. Our simulations qualitatively agree with the experimental observations of the photocatalytic conversion of CO_2 to CH_4. The maximum CH_4 yield of ~0.3 $\mu mol^{-1} \cdot g^{-1} \cdot h^{-1}$ for the 0.14Pt−0.6Cu composition, can be correlated with CO_2 activation and CH-intermediate formation. The photocatalytic performance degrades with a decrease of the density of interfacial sites, suggesting the necessity of an optimal surface area of interfacial regions for selective CO_2 conversion to hydrocarbons.

Comprehensive studies of several intermediate structures, together with the energetics and kinetics of many possible reaction pathways, shed light on the reaction mechanisms in detail. Nonetheless, exploring the PES of the main reactants (H_2O/CO_2) and several CH-containing intermediates with activation energy, vibrational entropy, and zero-point energy is computationally intensive and calls for future work. We hope that our studies encourage further studies on CuPt/P25 or similar systems and motivate the development of sophisticated MLIP potentials for the simulations of these photocatalytic systems with reactants and intermediates.

ASSOCIATED CONTENT

Supporting Information

The Supporting Information is available free of charge at https://pubs.acs.org/doi/10.1021/acs.jpcc.4c02275.

Additional figures (Figures S1−S12) and descriptions of methods and results; adsorption of CO_2 on a bare rutile TiO_2 surface; MLIP training and validation; exploration of potential energy surface; adsorption geometry of CuPt/TiO_2; CO_2 adsorption on CuPt/TiO_2; stability of CO; structures of reactants, intermediates, and products; experimental measurements (PDF)

AUTHOR INFORMATION

Corresponding Author

Takat B. Rawal − *Quantum Generative Materials (GenMat), Austin, Texas 78704, United States;* orcid.org/0000-0003-3191-7770; Email: takat.rawal@genmat.xyz

Authors

Vaidish Sumaria − *Quantum Generative Materials (GenMat), Austin, Texas 78704, United States; Caminosoft Technologies Inc., Simi Valley, California 93065, United States*

Young Feng Li − *Quantum Generative Materials (GenMat), Austin, Texas 78704, United States*

David Sommer − *Quantum Generative Materials (GenMat), Austin, Texas 78704, United States*

Jake Vikoren − *Quantum Generative Materials (GenMat), Austin, Texas 78704, United States*

Robert J. Bondi − *Quantum Generative Materials (GenMat), Austin, Texas 78704, United States*

Matthias Rupp − *Quantum Generative Materials (GenMat), Austin, Texas 78704, United States; Luxembourg Institute of Science and Technology (LIST), L-4362 Esch-sur-Alzette, Luxembourg*

Amrit Prasad − *Quantum Generative Materials (GenMat), Austin, Texas 78704, United States*

Deeptanshu Prasad − *Quantum Generative Materials (GenMat), Austin, Texas 78704, United States*

Complete contact information is available at: https://pubs.acs.org/10.1021/acs.jpcc.4c02275

Notes

The authors declare the following competing financial interest(s): We have filed a provisional patent relating to this work.

ACKNOWLEDGMENTS

We acknowledge Niraj Prasad for his valuable suggestions in setting up compute clusters on the AWS EC2 platform, which allowed us to run first-principles DFT calculations and train machine-learning models. We thank Alexander Imbault for reviewing the manuscript and providing comments. We would also like to acknowledge George Hathaway and Jun Cao at Hathaway Research International for their invaluable advice regarding this study's physical experimental efforts.

REFERENCES

(1) Haider, A. J.; Jameel, Z. N.; Al-Hussaini, I. H. M. Review on: Titanium Dioxide Applications. *Energy Procedia* **2019**, *157*, 17−29.

(2) Li, Z.; Li, Z.; Zuo, C.; Fang, X. Application of Nanostructured TiO_2 in UV Photodetectors: A Review. *Adv. Mater.* **2022**, *34*, No. e2109083.

(3) Mao, S.; Sun, B.; Ke, C.; Qin, J.; Yang, Y.; Guo, T.; Wu, Y. A.; Shao, J.; Zhao, Y. Evolution between CRS and NRS Behaviors in MnO_2@TiO_2 Nanocomposite Based Memristor for Multi-Factors-Regulated Memory Applications. *Nano Energy* **2023**, *107*, No. 108117.

(4) Wang, H.; Qi, H.; Sun, X.; Jia, S.; Li, X.; Miao, T. J.; Xiong, L.; Wang, S.; Zhang, X.; Liu, X.; Wang, A.; Zhang, T.; Huang, W.; Tang, J. High Quantum Efficiency of Hydrogen Production from Methanol Aqueous Solution with PtCu−TiO_2 Photocatalysts. *Nat. Mater.* **2023**, *22*, 619−626.

(5) Adachi, Y.; Brndiar, J.; Konôpka, M.; Turanský, R.; Zhu, Q.; Wen, H. F.; Sugawara, Y.; Kantorovich, L.; Štich, I.; Li, Y. J. Tip-Activated

Single-Atom Catalysis: CO Oxidation on Au Adatom on Oxidized Rutile TiO_2 Surface. *Sci. Adv.* **2023**, *9*, eadi4799.
(6) Bikondoa, O.; Pang, C. L.; Ithnin, R.; Muryn, C. A.; Onishi, H.; Thornton, G. Direct Visualization of Defect-Mediated Dissociation of Water on TiO_2(110). *Nat. Mater.* **2006**, *5*, 189−192.
(7) Galhenage, R. P.; Yan, H.; Rawal, T. B.; Le, D.; Brandt, A. J.; Maddumapatabandi, T. D.; Nguyen, N.; Rahman, T. S.; Chen, D. A. MoS_2 Nanoclusters Grown on TiO_2: Evidence for New Adsorption Sites at Edges and Sulfur Vacancies. *J. Phys. Chem. C* **2019**, *123*, 7185−7201.
(8) Park, J. B.; Ratliff, J. S.; Ma, S.; Chen, D. A. Understanding the Reactivity of Oxide-Supported Bimetallic Clusters: Reaction of NO with CO on TiO_2(110)-Supported Pt−Rh Clusters. *J. Phys. Chem. C* **2007**, *111*, 2165−2176.
(9) Yuan, W.; Zhu, B.; Li, X.-Y.; Hansen, T. W.; Ou, Y.; Fang, K.; Yang, H.; Zhang, Z.; Wagner, J. B.; Gao, Y.; Wang, Y. Visualizing H_2O Molecules Reacting at TiO_2 Active Sites with Transmission Electron Microscopy. *Science* **2020**, *367*, 428−430.
(10) Gao, C.; Wei, T.; Zhang, Y.; Song, X.; Huan, Y.; Liu, H.; Zhao, M.; Yu, J.; Chen, X. A Photoresponsive Rutile TiO_2 Heterojunction with Enhanced Electron−Hole Separation for High-Performance Hydrogen Evolution. *Adv. Mater.* **2019**, *31*, No. e1806596.
(11) Li, Z.; Wang, S.; Wu, J.; Zhou, W. Recent Progress in Defective TiO_2 Photocatalysts for Energy and Environmental Applications. *Renewable Sustainable Energy Rev.* **2022**, *156*, No. 111980.
(12) Schneider, J.; Matsuoka, M.; Takeuchi, M.; Zhang, J.; Horiuchi, Y.; Anpo, M.; Bahnemann, D. W. Understanding TiO_2 Photocatalysis: Mechanisms and Materials. *Chem. Rev.* **2014**, *114*, 9919−9986.
(13) Sorcar, S.; Hwang, Y.; Lee, J.; Kim, H.; Grimes, K. M.; Grimes, C. A.; Jung, J.-W.; Cho, C.-H.; Majima, T.; Hoffmann, M. R.; In, S.-I. CO_2, Water, and Sunlight to Hydrocarbon Fuels: A Sustained Sunlight to Fuel (Joule-to-Joule) Photoconversion Efficiency of 1%. *Energy Environ. Sci.* **2019**, *12*, 2685−2696.
(14) Lee, S.; Jeong, S.; Kim, W. D.; Lee, S.; Lee, K.; Bae, W. K.; Moon, J. H.; Lee, S.; Lee, D. C. Low-Coordinated Surface Atoms of CuPt Alloy Cocatalysts on TiO_2 for Enhanced Photocatalytic Conversion of CO_2. *Nanoscale* **2016**, *8*, 10043−10048.
(15) Sorcar, S.; Hwang, Y.; Grimes, C. A.; In, S.-I. Highly Enhanced and Stable Activity of Defect-Induced Titania Nanoparticles for Solar Light-Driven CO_2 Reduction into CH_4. *Mater. Today* **2017**, *20*, 507−515.
(16) Tasbihi, M.; Fresno, F.; Simon, U.; Villar-García, I. J.; Pérez-Dieste, V.; Escudero, C.; de la Peña O'Shea, V. A. On the Selectivity of CO_2 Photoreduction towards CH_4 Using Pt/TiO_2 Catalysts Supported on Mesoporous Silica. *Appl. Catal., B* **2018**, *239*, 68−76.
(17) Etacheri, V.; Valentin, C. D.; Schneider, J.; Bahnemann, D.; Pillai, S. C. Visible-Light Activation of TiO_2 Photocatalysts: Advances in Theory and Experiments. *J. Photochem. Photobiol., C* **2015**, *25*, 1−29.
(18) Amtout, A.; Leonelli, R. Optical Properties of Rutile near Its Fundamental Band Gap. *Phys. Rev. B* **1995**, *51*, 6842−6851.
(19) Scanlon, D. O.; Dunnill, C. W.; Buckeridge, J.; Shevlin, S. A.; Logsdail, A. J.; Woodley, S. M.; Catlow, C. R. A.; Powell, M. J.; Palgrave, R. G.; Parkin, I. P.; Watson, G. W.; Keal, T. W.; Sherwood, P.; Walsh, A.; Sokol, A. A. Band Alignment of Rutile and Anatase TiO_2. *Nat. Mater.* **2013**, *12*, 798−801.
(20) Liu, L.; Gao, F.; Zhao, H.; Li, Y. Tailoring Cu Valence and Oxygen Vacancy in Cu/TiO_2 Catalysts for Enhanced CO_2 Photoreduction Efficiency. *Appl. Catal., B* **2013**, *134-135*, 349−358.
(21) Acharya, D. P.; Camillone, N.; Sutter, P. CO_2 Adsorption, Diffusion, and Electron-Induced Chemistry on Rutile TiO_2(110): A Low-Temperature Scanning Tunneling Microscopy Study. *J. Phys. Chem. C* **2011**, *115*, 12095−12105.
(22) Sorescu, D. C.; Lee, J.; Al-Saidi, W. A.; Jordan, K. D. CO_2 Adsorption on TiO_2(110) Rutile: Insight from Dispersion-Corrected Density Functional Theory Calculations and Scanning Tunneling Microscopy Experiments. *J. Chem. Phys.* **2011**, *134*, No. 104707.
(23) Lin, X.; Yoon, Y.; Petrik, N. G.; Li, Z.; Wang, Z.-T.; Glezakou, V.-A.; Kay, B. D.; Lyubinetsky, I.; Kimmel, G. A.; Rousseau, R.; Dohnálek, Z. Structure and Dynamics of CO_2 on Rutile TiO_2(110)−1 × 1. *J. Phys. Chem. C* **2012**, *116*, 26322−26334.
(24) Zhao, C.; Xu, H. Activation of CO_2 by Direct Cleavage Triggered by Photoelectrons on Rutile TiO_2(110). *J. Phys. Chem. Lett.* **2023**, *14*, 1928−1933.
(25) Liu, L.; Zhao, H.; Andino, J. M.; Li, Y. Photocatalytic CO_2 Reduction with H_2O on TiO_2 Nanocrystals: Comparison of Anatase, Rutile, and Brookite Polymorphs and Exploration of Surface Chemistry. *ACS Catal.* **2012**, *2*, 1817−1828.
(26) Palfey, W. R.; Rossman, G. R.; Goddard, W. A. Structure, Energetics, and Spectra for the Oxygen Vacancy in Rutile: Prominence of the Ti−HO−Ti Bond. *J. Phys. Chem. Lett.* **2021**, *12*, 10175−10181.
(27) Kattel, S.; Yan, B.; Yang, Y.; Chen, J. G.; Liu, P. Optimizing Binding Energies of Key Intermediates for CO_2 Hydrogenation to Methanol over Oxide-Supported Copper. *J. Am. Chem. Soc.* **2016**, *138*, 12440−12450.
(28) Kar, P.; Zhang, Y.; Mahdi, N.; Thakur, U. K.; Wiltshire, B. D.; Kisslinger, R.; Shankar, K. Heterojunctions of Mixed Phase TiO_2 Nanotubes with Cu, CuPt, and Pt Nanoparticles: Interfacial Band Alignment and Visible Light Photoelectrochemical Activity. *Nanotechnology* **2018**, *29*, No. 014002.
(29) Kattel, S.; Yan, B.; Chen, J. G.; Liu, P. CO_2 Hydrogenation on Pt, Pt/SiO_2 and Pt/TiO_2: Importance of Synergy between Pt and Oxide Support. *J. Catal.* **2016**, *343*, 115−126.
(30) Qi, Y.; Yang, Z.; Jiang, Y.; Han, H.; Wu, T.; Wu, L.; Liu, J.; Wang, Z.; Wang, F. Platinum−Copper Bimetallic Nanoparticles Supported on TiO_2 as Catalysts for Photo−thermal Catalytic Toluene Combustion. *ACS Appl. Nano Mater.* **2022**, *5*, 1845−1854.
(31) Pang, C. L.; Lindsay, R.; Thornton, G. Chemical Reactions on Rutile TiO_2(110). *Chem. Soc. Rev.* **2008**, *37*, 2328−2353.
(32) Abraham, B. M.; Pique, O.; Khan, M. A.; Vines, F.; Illas, F.; Singh, J. K. Machine Learning−Driven Discovery of Key Descriptors for CO_2 Activation over Two−Dimensional Transition Metal Carbides and Nitrides. *ACS Appl. Mater. Interfaces* **2023**, *15*, 30117−30126.
(33) Mazheika, A.; Wang, Y.-G.; Valero, R.; Viñes, F.; Illas, F.; Ghiringhelli, L. M.; Levchenko, S. V.; Scheffler, M. Artificial-Intelligence-Driven Discovery of Catalyst Genes with Application to CO_2 Activation on Semiconductor Oxides. *Nat. Commun.* **2022**, *13*, No. 419.
(34) Mok, D. H.; Li, H.; Zhang, G.; Lee, C.; Jiang, K.; Back, S. Data-Driven Discovery of Electrocatalysts for CO_2 Reduction Using Active Motifs-Based Machine Learning. *Nat. Commun.* **2023**, *14*, No. 7303.
(35) Zhong, M.; Tran, K.; Min, Y.; et al. Accelerated Discovery of CO_2 Electrocatalysts Using Active Machine Learning. *Nature* **2020**, *581*, 178−183.
(36) Batzner, S.; Musaelian, A.; Sun, L.; Geiger, M.; Mailoa, J. P.; Kornbluth, M.; Molinari, N.; Smidt, T. E.; Kozinsky, B. E(3)−Equivariant Graph Neural Networks for Data−Efficient and Accurate Interatomic Potentials. *Nat. Commun.* **2022**, *13*, No. 2453.
(37) Musaelian, A.; Batzner, S.; Johansson, A.; Sun, L.; Owen, C. J.; Kornbluth, M.; Kozinsky, B. Learning Local Equivariant Representations for Large-Scale Atomistic Dynamics. *Nat. Commun.* **2023**, *14*, No. 579.
(38) Langer, M. F.; Goeßmann, A.; Rupp, M. Representations of Molecules and Materials for Interpolation of Quantum-Mechanical Simulations via Machine Learning. *npj Comput. Mater.* **2022**, *8*, No. 41.
(39) Xie, S. R.; Rupp, M.; Hennig, R. G. Ultra−Fast Interpretable Machine−Learning Potentials. *npj Comput. Mater.* **2023**, *9*, No. 162.
(40) Calegari Andrade, M. F.; Ko, H.-Y.; Zhang, L.; Car, R.; Selloni, A. Free Energy of Proton Transfer at the Water−TiO_2 Interface from Ab Initio Deep Potential Molecular Dynamics. *Chem. Sci.* **2020**, *11*, 2335−2341.
(41) Gupta, S.; Yang, X.; Ceder, G. What Dictates Soft Clay-like Lithium Superionic Conductor Formation from Rigid Salts Mixture. *Nat. Commun.* **2023**, *14*, No. 6884.
(42) Sumaria, V.; Nguyen, L.; Tao, F. F.; Sautet, P. Atomic-Scale Mechanism of Platinum Catalyst Restructuring under a Pressure of Reactant Gas. *J. Am. Chem. Soc.* **2023**, *145*, 392−401.

https://doi.org/10.1021/acs.jpcc.4c02275
J. Phys. Chem. C 2024, 128, 14247−14258

(43) Paleico, M. L.; Behler, J. Global Optimization of Copper Clusters at the ZnO(10−10) Surface Using a DFT−based Neural Network Potential and Genetic Algorithms. *J. Chem. Phys.* **2020**, *153*, No. 054704.
(44) Ko, T. W.; Finkler, J. A.; Goedecker, S.; Behler, J. A Fourth-Generation High-Dimensional Neural Network Potential with Accurate Electrostatics Including Non-local Charge Transfer. *Nat. Commun.* **2021**, *12*, No. 398.
(45) Sumaria, V.; Sautet, P. CO Organization at Ambient Pressure on Stepped Pt Surfaces: First Principles Modeling Accelerated by Neural Networks. *Chem. Sci.* **2021**, *12*, 15543−15555.
(46) Sun, G.; Sautet, P. Toward Fast and Reliable Potential Energy Surfaces for Metallic Pt Clusters by Hierarchical Delta Neural Networks. *J. Chem. Theory Comput.* **2019**, *15*, 5614−5627.
(47) Lim, J. S.; Vandermause, J.; Spronsen, M. A. v.; Musaelian, A.; Xie, Y.; Sun, L.; O'Connor, C. R.; Egle, T.; Molinari, N.; Florian, J.; Duanmu, K.; Madix, R. J.; Sautet, P.; Friend, C. M.; Kozinsky, B. Evolution of Metastable Structures at Bimetallic Surfaces from Microscopy and Machine−Learning Molecular Dynamics. *J. Am. Chem. Soc.* **2020**, *142*, 15907−15916.
(48) Vandermause, J.; Xie, Y.; Lim, J. S.; Owen, C. J.; Kozinsky, B. Active Learning of Reactive Bayesian Force Fields Applied to Heterogeneous Catalysis Dynamics of H/Pt. *Nat. Commun.* **2022**, *13*, No. 5183.
(49) Wen, B.; Andrade, M. F. C.; Liu, L.-M.; Selloni, A. Water Dissociation at the Water−Rutile TiO_2(110) Interface from Ab Initio−Based Deep Neural Network Simulations. *Proc. Natl. Acad. Sci. U.S.A.* **2023**, *120*, No. e2212250120.
(50) Jung, H.; Sauerland, L.; Stocker, S.; Reuter, K.; Margraf, J. T. Machine−Learning Driven Global Optimization of Surface Adsorbate Geometries. *npj Comput. Mater.* **2023**, *9*, No. 114.
(51) Bruix, A.; Margraf, J. T.; Andersen, M.; Reuter, K. First−Principles−Based Multiscale Modelling of Heterogeneous Catalysis. *Nat. Catal.* **2019**, *2*, 659−670.
(52) Schaaf, L. L.; Fako, E.; De, S.; Schäfer, A.; Csányi, G. Accurate Energy Barriers for Catalytic Reaction Pathways: An Automatic Training Protocol for Machine Learning Force Fields. *npj Comput. Mater.* **2023**, *9*, No. 180.
(53) Miyazaki, R.; Belthle, K. S.; Tuysuz, H.; Foppa, L.; Scheffler, M. Materials Genes of CO_2 Hydrogenation on Supported Cobalt Catalysts: An Artificial Intelligence Approach Integrating Theoretical and Experimental Data. *J. Am. Chem. Soc.* **2024**, *146*, 5433−5444.
(54) Kresse, G.; Furthmüller, J. Efficient Iterative Schemes for Ab Initio Total−Energy Calculations Using a Plane−Wave Basis Set. *Phys. Rev. B* **1996**, *54*, 11169−11186.
(55) Giannozzi, P.; Andreussi, O.; Brumme, T.; et al. Advanced Capabilities for Materials Modelling with Quantum ESPRESSO. *J. Phys.: Condens. Matter* **2017**, *29*, No. 465901.
(56) Perdew, J. P.; Burke, K.; Ernzerhof, M. Generalized Gradient Approximation Made Simple. *Phys. Rev. Lett.* **1996**, *77*, 3865−3868.
(57) Blöchl, P. E. Projector Augmented−Wave Method. *Phys. Rev. B* **1994**, *50*, 17953−17979.
(58) Rawal, T. B.; Le, D.; Rahman, T. S. MoS_2−supported Gold Nanoparticle for CO Hydrogenation. *J. Phys.: Condens. Matter* **2017**, *29*, No. 415201.
(59) Imaoka, T.; Kitazawa, H.; Chun, W. J.; Omura, S.; Albrecht, K.; Yamamoto, K. Magic Number Pt_{13} and Misshapen Pt_{12} Clusters: Which One Is the Better Catalyst? *J. Am. Chem. Soc.* **2013**, *135*, 13089−13095.
(60) Almeida, K.; Chagoya, K.; Felix, A.; Jiang, T.; Le, D.; Rawal, T. B.; Evans, P. E.; Wurch, M.; Yamaguchi, K.; Dowben, P. A.; Bartels, L.; Rahman, T. S.; Blair, R. G. Methanol Carbonylation to Acetaldehyde on Au Particles Supported by Single-Layer MoS_2 Grown on Silica. *J. Phys.: Condens. Matter* **2022**, *34*, No. 104005.
(61) Hong, S.; Rahman, T. S. Rationale for the Higher Reactivity of Interfacial Sites in Methanol Decomposition on Au_{13}/TiO_2(110). *J. Am. Chem. Soc.* **2013**, *135*, 7629−7635.
(62) Zhang, C.; Wang, Z.; Si, W.-D.; Wang, L.; Dou, J.-M.; Gao, Z.-Y.; Tung, C.-H.; Sun, D. Solvent-Induced Isomeric Cu_{13} Nanoclusters: Chlorine to Copper Charge Transfer Boosting Molecular Oxygen Activation in Sulfide Selective Oxidation. *ACS Nano* **2022**, *16*, 9598−9607.
(63) Luna, A. L.; Dragoe, D.; Wang, K.; Beaunier, P.; Kowalska, E.; Ohtani, B.; Uribe, D. B.; Valenzuela, M. A.; Remita, H.; Colbeau-Justin, C. Photocatalytic Hydrogen Evolution Using Ni−Pd/TiO_2: Correlation of Light Absorption, Charge-Carrier Dynamics, and Quantum Efficiency. *J. Phys. Chem. C* **2017**, *121*, 19449−19454.
(64) Bhuskute, B. D.; Ali-Löytty, H.; Honkanen, M.; Salminen, T.; Valden, M. Influence of the Photodeposition Sequence on the Photocatalytic Activity of Plasmonic Ag−Au/TiO_2 Nanocomposites. *Nanoscale Adv.* **2022**, *4*, 4335−4344.
(65) Vaida, M. E.; Rawal, T. B.; Bernhardt, T. M.; Marsh, B. M.; Rahman, T. S.; Leone, S. R. Nonmetal−to−Metal Transition of Magnesia Supported Au Clusters Affects the Ultrafast Dissociation Dynamics of Adsorbed CH_3Br Molecules. *J. Phys. Chem. Lett.* **2022**, *13*, 4747−4753.
(66) Brookes, I. M.; Muryn, C. A.; Thornton, G. Imaging Water Dissociation on TiO_2(110). *Phys. Rev. Lett.* **2001**, *87*, No. 266103.
(67) Wang, Z.-T.; Wang, Y.-G.; Mu, R.; Yoon, Y.; Dahal, A.; Schenter, G. K.; Glezakou, V.-A.; Rousseau, R.; Lyubinetsky, I.; Dohnálek, Z. Probing Equilibrium of Molecular and Deprotonated Water on TiO_2(110). *Proc. Natl. Acad. Sci. U.S.A.* **2017**, *114*, 1801−1805.
(68) Liu, X.; Xiao, J.; Peng, H.; Hong, X.; Chan, K.; Nørskov, J. K. Understanding Trends in Electrochemical Carbon Dioxide Reduction Rates. *Nat. Commun.* **2017**, *8*, No. 15438.
(69) Tang, Y.; Zhang, S.; Rawal, T. B.; Nguyen, L.; Iwasawa, Y.; Acharya, S. R.; Liu, J.; Hong, S.; Rahman, T. S.; Tao, F. Atomic−Scale Structure and Catalysis on Positively Charged Bimetallic Sites for Generation of H_2. *Nano Lett.* **2020**, *20*, 6255−6262.
(70) Yu, Y.; Dong, X.; Chen, P.; Geng, Q.; Wang, H.; Li, J.; Zhou, Y.; Dong, F. Synergistic Effect of Cu Single Atoms and Au−Cu Alloy Nanoparticles on TiO_2 for Efficient CO_2 Photoreduction. *ACS Nano* **2021**, *15*, 14453−14464.
(71) Allegretti, F.; O'Brien, S.; Polcik, M.; Sayago, D. I.; Woodruff, D. P. Adsorption Bond Length for H_2O on TiO_2(110): A Key Parameter for Theoretical Understanding. *Phys. Rev. Lett.* **2005**, *95*, No. 226104.
(72) Schaub, R.; Thostrup, P.; Lopez, N.; Lægsgaard, E.; Stensgaard, I.; Nørskov, J. K.; Besenbacher, F. Oxygen Vacancies as Active Sites for Water Dissociation on Rutile TiO_2(110). *Phys. Rev. Lett.* **2001**, *87*, No. 266104.
(73) Muttaqien, F.; Hamamoto, Y.; Hamada, I.; Inagaki, K.; Shiozawa, Y.; Mukai, K.; Koitaya, T.; Yoshimoto, S.; Yoshinobu, J.; Morikawa, Y. CO_2 Adsorption on the Copper Surfaces: Van Der Waals Density Functional and TPD Studies. *J. Chem. Phys.* **2017**, *147*, No. 094702.
(74) Liu, X.; Sun, L.; Deng, W.-Q. Theoretical Investigation of CO_2 Adsorption and Dissociation on Low Index Surfaces of Transition Metals. *J. Phys. Chem. C* **2018**, *122*, 8306−8314.
(75) Barlocco, I.; Maleki, F.; Pacchioni, G. CO_2 Activation on Cu/TiO_2 Nanostructures: Importance of Dual Binding Site. *Chem. - Eur. J.* **2023**, *29*, No. e202300757.

https://doi.org/10.1021/acs.jpcc.4c02275
J. Phys. Chem. C 2024, 128, 14247−14258